

# Chapter 1

## Theory

### 1.1 X-ray Diffraction Principles

#### 1.1.1 Scattering at Lattices

To elucidate the working principles behind X-ray diffraction (XRD) as a measurement method (cf. 2.2.5), a brief description of reciprocal space and constructive interference will be provided. Those derivations are based on Ashcroft and Mermin (1976) [1].

A periodic point-like structure with translational symmetry (“BRAVAIS lattice”) can be described by three vectors  $\mathbf{a}_i$  that span a so-called “unit cell”. Every lattice point  $\mathbf{R}$  is a linear combination of those unit cell vectors. For such a lattice, there exists a so-called “reciprocal lattice”, which consists of all vectors  $\mathbf{K}$  satisfying the condition<sup>1</sup>:

$$e^{i\langle \mathbf{K}, \mathbf{R} \rangle} = 1. \quad (1.1)$$

This is again a BRAVAIS lattice with unit cell vectors  $\mathbf{a}_j^*$ :

$$\mathbf{K}_{hkl} = h\mathbf{a}_1^* + k\mathbf{a}_2^* + l\mathbf{a}_3^*. \quad (1.2)$$

It follows that for any  $i, j$ :

$$\langle \mathbf{a}_i^*, \mathbf{a}_j \rangle = 2\pi\delta_{ij}, \quad (1.3)$$

with the KRONECKER delta  $\delta_{ij}$ . A major application of reciprocal space vectors is their ability to describe lattice planes. Any lattice plane can be described by the shortest possible reciprocal space vector  $\mathbf{K}_{hkl}$  perpendicular to it. Consequently, the lattice plane is denoted by  $(hkl)$ . The distance between equivalent lattice planes can be calculated via

$$d_{hkl} = |\mathbf{K}_{hkl}|^{-1}. \quad (1.4)$$

Note that for non-cubic crystals, the lattice plane  $(hkl)$  is in general *not* perpendicular to the lattice direction  $[hkl]$ .

With those preliminaries, the conditions for constructive interference during diffraction of radiation at BRAVAIS lattices can be derived. Consider two scattering centers separated by  $\mathbf{d}$ . Now consider incoming radiation with wave vector  $\mathbf{k}$ :

$$\mathbf{k} = \frac{2\pi}{\lambda} \hat{\mathbf{n}}, \quad (1.5)$$

---

<sup>1</sup>The definition of  $\mathbf{K}$  by (1.1) is a consequence of demanding that the plane wave described by  $f_{\mathbf{K}}(\mathbf{r}) = \exp(i\langle \mathbf{K}, \mathbf{r} \rangle)$  has the same symmetry as the BRAVAIS lattice [1].

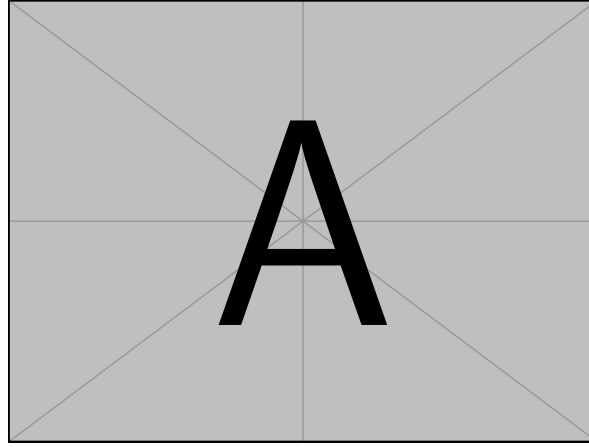


**Figure 1.1:** Here comes an ashcroft-like image for the scattering geometry to derive Equ. (1.6)

with wavelength  $\lambda$  and direction  $\hat{\mathbf{n}}$ . For the case of elastic scattering, the outgoing wave vector  $\mathbf{k}'$  has the same wavelength  $\lambda$  but different direction  $\hat{\mathbf{n}}'$ . The phase difference of two photons scattered at the 1st and 2nd scattering center, respectively, can be calculated from their path difference, which reads

$$\langle \mathbf{d}, \hat{\mathbf{n}} \rangle + \langle -\mathbf{d}, \hat{\mathbf{n}}' \rangle. \quad (1.6)$$

Constructive interference occurs, if the phase difference is an integral multiple of the wavelength, so it must follow that

$$\langle \mathbf{d}, (\hat{\mathbf{n}} - \hat{\mathbf{n}}') \rangle = m\lambda \quad (1.7)$$

$$\Leftrightarrow \langle \mathbf{d}, (\hat{\mathbf{k}} - \hat{\mathbf{k}}') \rangle = 2\pi m, \quad (1.8)$$

with  $m \in \mathbb{N}$ . Comparing with (1.1) reveals that  $\hat{\mathbf{k}} - \hat{\mathbf{k}}'$  is a reciprocal space vector, because the separation  $\mathbf{d}$  of the two scattering centers is a lattice vector. So constructive interference (observing a reflex) occurs if and only if the scattering geometry (determined by angle of incidence and refraction, as well as wavelength) matches the lattice symmetry in the sense that there is a corresponding lattice translation vector  $\mathbf{d}$  fulfilling Equ. (1.8). So from the “position” of reflexes, one can deduce the lattice symmetry.

Note that this description of X-ray scattering is equivalent to the BRAGG condition:

$$m\lambda = 2d_{hkl} \sin(\theta), \quad (1.9)$$

where the angle of incidence  $\theta$  and  $\lambda$  are contained in  $\hat{\mathbf{k}} - \hat{\mathbf{k}}'$ . Furthermore, when a lattice point is not equivalent to a single atom, but represents several scattering centers, an additional geometrical structure factor has to be taken into account to determine whether a certain geometry allows reflexes. This is important, e.g., for structures with trigonal symmetry. They are described with a conventional hexagonal unit cell, although not every plane ( $hkl$ ) exhibits constructive interference.

### 1.1.2 X-rays

Atomic distances in solids are of the order of several Å, so the radiation for probing those structures must have a similar wavelength, which turns out to be X-rays [2]. The following description of X-rays is based on Spieß (2009) [3].

The basis of any X-ray tube are high-energy electrons which are produced by thermionic emission in a cathode, which is usually made out of tungsten<sup>2</sup>. An electric field of several kV accelerates the electrons to the anode, where they are stopped such that around 99 % of their kinetic energy dissipates. The momentum change of electrons, which are charged particles, leads to emission of *bremssstrahlung*. Furthermore, the electrons ionize atoms of the anode material which leads to unoccupied electron states. If those states are filled by electrons with higher quantum number  $n$ , the difference in energy of those levels is emitted as radiation with a discrete spectrum, called characteristic X-ray. Important for this work is a part of the characteristic spectrum, called K-radiation, which originates in occupation of empty  $1s$ -orbitals. The occupying electron must come from an orbital with angular momentum quantum number  $l = 1$ , i.e. a  $p$ -orbital, because  $\Delta l$  cannot be zero. The radiation is termed  $K\alpha$ - or  $K\beta$ -radiation, if the previous orbital was  $2p$  or  $3p$ , respectively. Furthermore, one distinguishes  $K\alpha_1$ - and  $K\alpha_2$ -radiation, depending on the magnetic quantum number of the previous orbital, which can be  $\frac{3}{2}$  or  $\frac{1}{2}$ , respectively.  $K\alpha$ -radiation is desired for probing crystal structures.

## 1.2 Sesquioxides

Transparent Conductive Oxides (TCOs) are materials that combine the properties of having low absorption coefficient in the visible spectrum and being conductive at the same time [4]. The interest in these materials is motivated by possible usage in portable and flexible electronics, displays, solar cells and more [5]. Due to the restriction on only a few materials in the industry (e.g.  $\text{SnO}_2$  and  $\text{In}_2\text{O}_3$ ), investigations of new materials are required [5]. This includes fabrication of  $p$ -type TCOs as well as compounds with even larger band gaps than 3 eV, called Ultrawide-bandgap (UWBG) materials. A candidate for the latter is  $\text{Ga}_2\text{O}_3$  with its several polymorphs [6], where the corundum structured  $\alpha$ - $\text{Ga}_2\text{O}_3$  gained interest, even though its deposition has to account for parasitic growth of the thermodynamically more stable  $\beta$ -phase [7].

At this point,  $\text{Cr}_2\text{O}_3$  comes in handy being a possible  $p$ -type TCO as well as being isomorphic to group-III sesquioxide  $\alpha$ - $\text{Ga}_2\text{O}_3$  with quite similar lattice parameters (cf. Tab. 1.1). This enables the use of  $\text{Cr}_2\text{O}_3$  as a buffer layer between  $\alpha$ - $\text{Ga}_2\text{O}_3$  and isomorphic  $\alpha$ - $\text{Al}_2\text{O}_3$  (sapphire) substrates to improve the deposition process [8]. Furthermore,  $\text{Cr}_2\text{O}_3$  exhibits increased conductivity upon doping [9] and could thus serve as  $p$ -type component in a  $p$ - $n$ -heterojunction with  $\alpha$ - $\text{Ga}_2\text{O}_3$ . In the following, an overview of the two mentioned sesquioxides will be provided with focus on the physical properties being relevant to this work.

### 1.2.1 Chromium Oxide

“Chromia” or “Eskolaite” is a sesquioxide composed of the transition metal chromium and oxygen with formula unit  $\text{Cr}_2\text{O}_3$ . Among other chromium oxides (e.g. metallic  $\text{CrO}_2$ , toxic  $\text{CrO}_3$  etc.), it is the thermodynamically most stable phase [10–12], making it the abundant chromium oxide on earth [13].  $\text{Cr}_2\text{O}_3$  occurs mainly in the  $\alpha$ -phase

---

<sup>2</sup>Tungsten is the element with the second highest melting point of around 3400 °C. This ensures a low contamination of the anode with cathode material.

	$a$	$c$	Ref.
$\alpha$ -Al <sub>2</sub> O <sub>3</sub>	4.76 Å	13.00 Å	Pishchik et al. (2009) [20]
$\alpha$ -Cr <sub>2</sub> O <sub>3</sub>	4.96 Å	13.59 Å	Mi et al. (2018) [13]
$\alpha$ -Ga <sub>2</sub> O <sub>3</sub>	4.98 Å	13.43 Å	Marezio and Remeika (1967) [21]

**Table 1.1:** Lattice constants of selected corundum structured compounds.

(described below), but a cubic spinel  $\gamma$ -phase with random missing Cr point defects has also been reported [10]. Henceforth, “Cr<sub>2</sub>O<sub>3</sub>” will refer to the  $\alpha$ -phase.

As coating material, Cr<sub>2</sub>O<sub>3</sub> is commonly used due to its high hardness and resistance against corrosion [11, 14], also explaining its use-case as component of stainless steel to form passive films [12]. Cr<sub>2</sub>O<sub>3</sub> thin films absorb electromagnetic waves with wavelengths smaller than 400 nm, making it opaque in the UV-spectrum [15, 16]. It is transparent in the visible spectrum with, e.g., a reported transmittance of 40 % at 700 nm for 0.5  $\mu$ m thick films by Cheng et al. (1996) [15].

Cr<sub>2</sub>O<sub>3</sub> crystallizes in the corundum structure, which has trigonal symmetry (space group  $R\bar{3}c$ ) and belongs to the hexagonal crystal family. One unit cell contains six formula units, i.e. 12 chromium cations and 18 oxygen anions [12]. The oxygen atoms arrange in a hexagonal close-packed manner, where two thirds of the formed octahedrons are filled with Cr atoms [17]. The unit cell is spanned by a principal axis, called  $c$ -axis<sup>3</sup>, and a hexagonal basal plane with lattice constant  $a$ . The numerical values for those lattice parameters differ depending on the publication [4, 8, 13, 18, 19], and we will use the values in Tab. 1.1.

Several techniques were applied for depositing chromia thin films, including: Chemical Vapor Deposition (CVD) [22–24] on silicon and glass, Molecular Beam Epitaxy (MBE) on sapphire [4, 25], thermal evaporation on platinum [10], electron-beam evaporation on glass [11], spray pyrolysis on glass [26], radio-frequency (RF) sputtering on sapphire [8, 27, 28], reactive direct current (DC) sputtering on glass [16], reactive Pulsed Laser Deposition (PLD) on silicon [29] and sapphire [30], and non-reactive PLD on sapphire [4, 14, 31].

**Electronic Structure** Experimental and theoretical studies reveal that chromia exhibits a band gap of 3.2–3.4 eV [10, 12, 13, 19] making it a wide band gap material. This predicts insulating behavior [19], classified as both Mott-Hubbard type and charge-transfer type, which are models to describe the electronic behavior of compounds containing transition metals with partly filled  $3d^n$  orbitals<sup>4</sup> [12, 13, 17]: Density Functional Theory (DFT) calculations show that the Cr-3d states are almost solely responsible for electronic states in the conduction band and that they are also present in the valence band [12, 13]. Thus,  $3d \rightarrow 3d$  band transitions are possible, favoring the Mott-Hubbard model of this compound [12]. Furthermore, the O-2p states are mainly present in the valence band, at similar energies as the Cr-3d states, which leads to hybridization and thus favoring the charge-transfer model [12].

<sup>3</sup>The spins of the Cr atoms along this direction are alternating  $3 \uparrow$  and  $3 \downarrow$  [4], making the crystal antiferromagnetic [12, 17].

<sup>4</sup> $n = 5$  for Cr

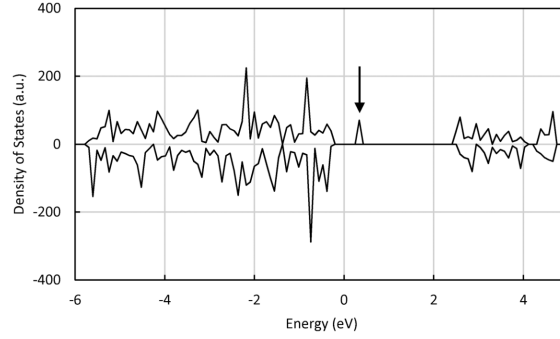


**Figure 1.2:** Calculated density of states (DOS) of chromia, taking a  $V_{\text{Cr}}$  into account. The arrow marks the new acceptor level. Image taken from [12].

However, several studies agree on  $\text{Cr}_2\text{O}_3$  being a semiconductor with  $p$ -type conductivity<sup>5</sup> at room temperature and atmospheric conditions [12–15, 27, 29, 32]. Calculating the impact of different crystal point defects on the band structure may give insight into these observations. Indeed, when considering a missing chromium atom (“vacancy”  $V_{\text{Cr}}$ ) the band structure changes in two ways: The band gap itself is reduced [13], but not in a way that it would make excitations of valence electrons into the conduction band much more probable than for defectless chromia. But additionally, there is a new band introduced slightly above the Fermi level (cf. Fig. 1.2), which acts as an unoccupied acceptor level [13]. This defect state is mainly composed of O-2*p* orbitals of the oxygen anions surrounding the vacancy [12]. From a more intuitive point of view, a missing neutral chromium atom effectively removes the  $\text{Cr}^{3+}$  cation as well as three electrons bound to the adjacent  $\text{O}^{2-}$  anions, thus creating three holes [12] explaining the  $p$ -type conductivity.

Note that there are also other possible defects with different effects: a chromium Frenkel point defect describes a Cr atom leaving its position and occupying a formerly unoccupied cavity in one of the oxygen-octahedrons. This Frenkel defect actually creates a new band right below the Fermi level, acting as an occupied donor level [12]. A similar defect state is introduced by oxygen vacancies [13]. But note that the Fermi level is located only slightly above the Valence Band Maximum (VBM) and thus the new occupied donor level is not significantly closer to the Conduction Band Minimum (CBM), which means that electrons still have to overcome the band gap energy to get into conducting states. This favors the formation of holes via Cr vacancies (O-2*p* acceptor states) rather than electrons via Cr Frenkel defects and O vacancies (Cr-3*d* donor states).

**Doping** Several attempts have been made to alter the conductivity of chromia thin films deliberately, including incorporation of magnesium, nickel, or lithium to achieve better  $p$ -type conductivity [25]. On the other hand, incorporating titanium seems to yield electrons as majority carriers [33] due to the higher valent state of Ti when substituting Cr sites ( $\text{Ti}_{\text{Cr}}$ ) [32].

<sup>5</sup>Cheng et al. (2001) [23] actually find  $\text{Cr}_2\text{O}_3$  to be insulating. It is noted that they examined  $\text{Cr}_2\text{O}_3$  as an 2 nm thick oxide surface on  $\text{CrO}_2$  films deposited by CVD. Farrell et al. (2015) [25] also find that their high quality epitaxial films of  $\text{Cr}_2\text{O}_3$  grown by MBE exhibit no  $p$ -type conductivity. Similar results were found by Kehoe et al. (2016) [4] for MBE and PLD deposited films.

Due to interest in the electrical properties of *p*-type TCOs, the influence on Mg-doped  $\text{Cr}_2\text{O}_3$  thin films has been investigated by several studies [4, 9, 19, 25, 26, 31, 33]. Substituting Cr atoms with less valent hole providers – compared to structural defects of pure  $\text{Cr}_2\text{O}_3$  – does not only allow for a more controlled defect incorporation, but is also energetically more favorable due to a lower formation energy of  $\text{Mg}_{\text{Cr}}$  compared to  $V_{\text{Cr}}$  [4]. Uekawa and Kaneko (1996) [9] report an increase in conductivity of five orders of magnitude for  $\text{Cr}_2\text{O}_3\text{:Mg}$  thin films. This result can be further improved by postannealing [25] and deposition at higher oxygen partial pressures [25, 33]. These effects are attributed to homogenization of magnesium inside the thin films and increased MgO incorporation during deposition, respectively. An observed side-effect of Mg-doping is a color change to a brownish tint [9, 19]. Uekawa and Kaneko (1996) [9] discuss that this may be the result of a mixed valence state of chromium ( $\text{Cr}^{4+}$  or  $\text{Cr}^{6+}$ ), formed upon doping, as observed by X-ray Photoelectron Spectroscopy (XPS). This may establish an unoccupied state, favoring charge-transfer transitions from O-2*p* orbitals to this low-energetic state, resulting in a different visual appearance of the thin films. However, it has been shown that the overall transparency can be increased by codoping of Mg with nitrogen which also reduces the decolorization substantially [19, 26].

## 1.2.2 Gallium Oxide

$\text{Ga}_2\text{O}_3$  is a group-III sesquioxide with four different polymorphs, of which  $\beta\text{-Ga}_2\text{O}_3$  is the thermodynamically most stable one at ambient conditions [6, 7, 34]. The corundum-structured  $\alpha\text{-Ga}_2\text{O}_3$  phase, which is of more relevance for this work, is isomorphic to  $\text{Cr}_2\text{O}_3$  (cf. section 1.2.1), with lattice parameters as listed in Tab. 1.1.  $\alpha\text{-Ga}_2\text{O}_3$  is metastable [35], i.e. not favored in the first place, but remains irreversibly after formation, e.g., after phase transition from  $\beta$ - to  $\alpha$ -phase at high temperatures [36]. The thermodynamic equilibrium – which determines the favored phase – can also be changed by strain due to lattice mismatch occurring during heteroepitaxy<sup>6</sup> [34]. This approach is of particular interest due to the possibility of deposition on cheap<sup>7</sup> and readily available sapphire substrates which are isomorphic to  $\alpha\text{-Ga}_2\text{O}_3$  [28, 35, 36]. Note that deposition of  $\beta\text{-Ga}_2\text{O}_3$  on sapphire is also possible, but only with restriction to formation of more than one crystal domain [37]. On the other hand, highly crystalline [36]  $\alpha\text{-Ga}_2\text{O}_3$  thin films should be able to be grown without rotational domains [37].

Deposition of  $\alpha\text{-Ga}_2\text{O}_3$  on sapphire has been done by several deposition techniques, including [37]: Halide Vapor Phase Epitaxy (HVPE), mist CVD [38], MBE [34], Atomic Layer Deposition and metalorganic CVD. Phase-pure deposition via PLD has also been achieved [7, 34]. Despite being isomorphic to each other,  $\alpha\text{-Ga}_2\text{O}_3$  and sapphire still exhibit a lattice mismatch of around 4.8% along the *a*-axis [35]. This induces semi-coherent growth with a fairly high dislocation density, which has been reported to be around  $7 \times 10^{10} \text{ cm}^{-2}$  [38]. In particular, this becomes a problem regarding carrier mobility which is tremendously hindered by dislocation scattering [35].

To overcome the problems of lattice mismatch between sapphire substrates and  $\alpha\text{-Ga}_2\text{O}_3$  thin films, quasi-continuous gradients from  $\text{Al}_2\text{O}_3$  to  $\alpha\text{-Ga}_2\text{O}_3$  have been applied,

<sup>6</sup>However, the possibility of formation of parasitic  $\beta$ -phase still has to be taken into account [7].

<sup>7</sup>Compared to bulk  $\beta\text{-Ga}_2\text{O}_3$  substrates [35, 37].

utilizing the capability of alloying the respective compounds [39]. Furthermore, buffer layers of isomorphic  $\text{Cr}_2\text{O}_3$  have been used to decrease the high dislocation density for deposition on  $c$ -oriented [8, 27] as well as  $r$ -oriented sapphire [28]. Deposition on other than  $c$ -oriented substrates also seems to decrease parasitic phases, because the suppression of crystal facets perpendicular to the principal  $c$ -axis may increase phase purity [40]. It has to be noted that despite the difficulties occurring upon lattice mismatch, coherent growth seems to be feasible without buffer layers for different deposition techniques, at least for some monolayers [34].

With 5.0–5.3 eV [37],  $\alpha\text{-Ga}_2\text{O}_3$  has the highest band gap of the four polymorphs [36]. Increasing or decreasing the band gap is possible by alloying with  $\text{Al}_2\text{O}_3$  [40] or  $\text{In}_2\text{O}_3$  [41], respectively. The crystal structure also allows for alloying with other corundum structured compounds [37], in particular other transition metal oxides such as  $\text{Cr}_2\text{O}_3$  [27, 28]. The conduction band is mainly composed of Ga-4s states with an effective electron mass of  $0.3m_e$ . The valence band is very flat and mainly composed of O-2p orbitals, yielding a high effective electron mass and thus strong localization [36]. Next to band gap engineering,  $n$ -type doping via Sn or Si incorporation has been accomplished [37].

## 1.3 Heteroepitaxy

### 1.3.1 Pseudomorphic Growth

Comment: Ist der folgende Absatz zu lang, dafür dass ich (wahrscheinlich) nur bei  $c$ -Orientierung pseudomorphic growth beobachte? Aber ich wollte gerne ausrechnen, was denn der out of plane strain wäre, falls es so sein sollte, damit ich später argumentieren kann, ob ich relaxed oder pseudomorphic beobachte; oder was dazwischen. Dementsprechend hab ich mich dann gezwungen gefühlt, das ganze noch mal aufzurollen. Vielleicht wäre eine Lösung, (1.11), (1.12) und (1.13) in eine Art appendix zu tun?

When a body is deformed (“strained”) from its original state of equilibrium (“bulk”), forces will arise that tend to return the body to this equilibrium. Molecular forces are the driving element behind these so-called stresses [42]. In continuum mechanics, stress  $\sigma_{ij}$  and strain  $\epsilon_{kl}$  are symmetric rank-2 tensors that are linearly connected by the elasticity tensor with components  $C_{ijkl}$ :

$$\sigma_{ij} = C_{ijkl}\epsilon_{kl}, \quad (1.10)$$

which represents a set of linear equations<sup>8</sup>.

If the in-plane ( $ip$ ) lattice constants of two isomorphic compounds match at the interface of a heterostructure, one refers to “pseudomorphic” growth. This case confines some equations of (1.10):

1. The thin film  $ip$  lattice constants have to match the substrate  $ip$  lattice constants. This defines the magnitude of  $ip$  strain of the thin film material.

---

<sup>8</sup>Summation over same indices.



**Table 1.2:** The six independent entries of the elasticity tensor for rhombohedral  $\text{Cr}_2\text{O}_3$  [44] and  $\alpha\text{-Ga}_2\text{O}_3$  [43]. All values are in units of 100 GPa.

Material	$C_{11}$	$C_{12}$	$C_{13}$	$C_{33}$	$C_{44}$	$C_{14}$
$\alpha\text{-Cr}_2\text{O}_3$	3.74	1.48	1.75	3.62	1.59	-0.19
$\alpha\text{-Ga}_2\text{O}_3$	3.82	1.74	1.26	3.46	0.78	-0.17

2. On the other hand, due to vertical growth, the out-of-plane (*oop*) stress of the thin film is demanded to be zero.

The resulting *oop* strain as well as non-diagonal strain components can be derived by solving the system of equations (1.10) with these two boundary conditions. In Ref. [43], formulas are derived for the unknown strains in the special case of pseudomorphic heterostructures with threefold rhombohedral symmetry. For numerical predictions of those strains, the elasticity tensor  $C_{ijkl}$  of the thin film compound has to be known. Depending on the symmetry of the crystal structure, its components collapse into a lower number of independent entries<sup>9</sup>: for rhombohedral crystals, six independent components are left [1]. An example of the entries of the elasticity tensor for two sesquioxides is given in Tab. 1.2.

Because of its direct influence on the *oop* lattice plane distance and thus on the XRD patterns (cf. 1.1.2), the strain component perpendicular to the sample surface,  $\epsilon_{zz}$ , is of particular interest. In the following, the relevant formulas are stated as derived in Ref. [43]. They depend on the respective *ip* strains  $\epsilon_{xx}$  and  $\epsilon_{yy}$  caused by the lattice mismatch between film and substrate. Note that here,  $\mathbf{r} = (x, y, z)$  describes coordinates in the laboratory system – in contrary to Ref. [43], where  $\mathbf{r}$  and  $\mathbf{r}'$  are used to describe cartesian coordinates in the crystal and laboratory system, respectively.

One derives for (11.0)-plane (*a*-orientation):

$$\epsilon_{zz,a} = -\frac{C_{13}\epsilon_{xx,a} + C_{12}\epsilon_{yy,a}}{C_{11}}, \quad (1.11)$$

for (10.0)-plane (*m*-orientation):

$$\epsilon_{zz,m} = -\frac{C_{13}C_{44}\epsilon_{xx,m} + (C_{12}C_{44} + C_{14}^2)\epsilon_{yy,m}}{C_{11}C_{44} - C_{14}^2}, \quad (1.12)$$

and for (00.1)-plane (*c*-orientation):

$$\epsilon_{zz,c} = -\frac{2C_{13}}{C_{33}}\epsilon_{yy,c}, \quad (1.13)$$

with  $\epsilon_{xx,a} = c_S/c_F - 1$  and  $\epsilon_{yy,a} = a_S/a_F - 1$ , depending on the lattice parameters of substrate ( $a_S, c_S$ ) and film ( $a_F, c_F$ ). Note that

$$\begin{aligned} \epsilon_{xx,a} &= \epsilon_{xx,m}, \\ \epsilon_{yy,a} &= \epsilon_{yy,m}, \\ \epsilon_{yy,c} &= \epsilon_{yy,a}. \end{aligned}$$

<sup>9</sup>Due to symmetry reasons [1], the nine indices  $ij$  of the strain tensor can be unambiguously expressed by one index with six possible values:  $11 \rightarrow 1, 22 \rightarrow 2, 33 \rightarrow 3, 23 \rightarrow 4, 13 \rightarrow 5, 12 \rightarrow 6$  [43]. This allows for a  $6 \times 6$ -matrix representation of the elasticity tensor  $C_{ijkl} \rightarrow C_{\mu\nu}$ .



**Table 1.3:** (a) Comparison of  $d$  and  $d_{\text{str}}$ , which are the *oop* lattice plane distances for bulk  $\text{Cr}_2\text{O}_3$  and pseudomorphic  $\text{Cr}_2\text{O}_3$  on  $\text{Al}_2\text{O}_3$ , respectively. The corresponding *oop*-strain  $\epsilon_{zz}$  is also given, as well as the corresponding angles of reflection for  $2\theta$ - $\omega$ -scans. (b) The resulting tilt of the thin film depending on substrate orientation for relaxed growth. The results follow from considerations on the possible slip systems and BURGER’s vectors.

Orientation (X-ray reflection)	(a) Pseudomorphic					(b) Relaxed	
	$d$ (nm)	$d_{\text{str}}$ (nm)	$\epsilon_{zz}(\%)$	$2\theta$ ( $^\circ$ )	$2\theta_{\text{str}}$ ( $^\circ$ )	$\theta_{T,x}$	$\theta_{T,y}$
$c$ (00.6)	13.59	14.12	3.90	39.75	38.20	–	–
$a$ (11.0)	2.48	2.57	3.63	36.18	34.87	no	no
$m$ (30.0)	4.30	4.45	3.67	65.06	62.49	yes	no
$r$ (02.4)	3.63	3.72	2.41	50.19	48.93	yes	no

For (01.2)-plane ( $r$ -orientation), the formula gets longer and can be calculated as demonstrated in Grundmann (2020) [45]. The distance of lattice planes  $d$  orthogonal to the sample surface are then strained, such that:

$$d_{\text{strained}} = d(1 + \epsilon_{zz}). \quad (1.14)$$

Assuming pseudomorphic growth of  $\text{Cr}_2\text{O}_3$  on  $\text{Al}_2\text{O}_3$ , one can compare the strained lattice plane distances to the unstrained bulk values, by utilizing (1.14). The numerical values, calculated from the lattice constants (Tab. 1.1) and the elasticity tensor (Tab. 1.2), are listed in Tab. 1.3a.

### 1.3.2 Relaxed Growth

#### Dislocations

When the lattice mismatch is not resolved by adaption to the substrate (cf. 1.3.1), the periodicity of the film must be disrupted via so-called dislocations to facilitate relaxed growth of the film [46]. The highest disturbance from equilibrium spacing happens close to the so-called dislocation line which draws through the material – far away from this line, the crystallinity is restored. In which fashion the distortion happens, can be characterized by the BURGER’s vector  $\mathbf{b}$ . The relation of the BURGER’s vector to the dislocation line determines the type of the dislocation: if they are orthogonal, one refers to an *edge* dislocation; if they are parallel, one refers to a *screw* dislocation. For a so-called “perfect” dislocation<sup>10</sup>, the BURGER’s vector is a lattice translation vector. Note that in general, dislocations exhibit both edge- and screw-character [48].

Dislocations are not static, but can move (“glide”) inside the crystal. The movement happens typically inside a plane which has highest density of atoms (“glide plane”) and along the BURGER’s vector which is responsible for the dislocation [48]. The arrangement of glide plane and direction of movement is called “slip system”, e.g. for hexagonal structures, one finds  $\{00.1\}/(11.0)$  to be one prevailing slip system [48].

<sup>10</sup>Also referred to as “full” dislocation [47].

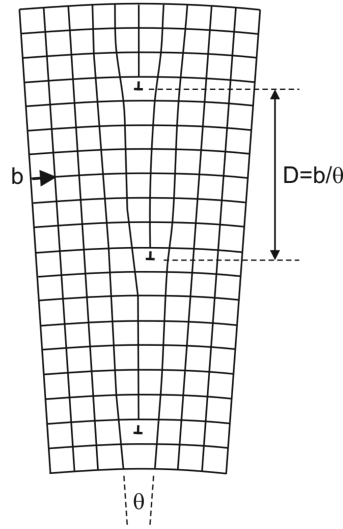


**Figure 1.3:** Edge dislocation with BURGER’s vector perpendicular to sample surface. The normal to the surface draws horizontally in this picture. Taken from Grundmann (2016) [47] tbd

For heterostructures with certain slip systems, the relaxation results in an additional tilt of the deposited film. This happens because a BURGER’s vector  $\mathbf{b}$  has more than one component: the edge component  $b_{\parallel}$  causes strain relaxation along  $b_{\parallel}$ ; but if  $\mathbf{b}$  also exhibits a component  $b_{\perp}$  orthogonal to the sample surface and the dislocation line, a tilt angle  $\theta_T$  will result between substrate and relaxed film:

$$\theta_{T,i} = \epsilon_{ii} \frac{b_{i,\perp}}{b_{i,\parallel}}, \quad (1.15)$$

where  $i$  denotes the axis of strain relaxation. This is schematically depicted in Fig. 1.3.

### Slip Systems for Sesquioxide Heterostructures

For heteroepitaxial  $(\text{Al}_x\text{Ga}_{1-x})_2\text{O}_3\text{-Al}_2\text{O}_3$  systems with low Al content, studies have been conducted on the prevailing relaxation mechanisms for  $r$ -oriented [49, 50], as well as  $a$ - and  $m$ -oriented [46] growth directions. In the following, those results will be summarized. Note that the  $x$ -axis points along the  $c$ -axis for  $m$ - and  $a$ -oriented heterostructures, and similarly along the projection of the  $c$ -axis on the sample surface for  $r$ -oriented heterostructures.

**(01.2)-plane ( $r$ -orientation)** The two relevant slip systems are  $\{00.1\}/\frac{1}{3}\langle 11.0 \rangle$  and  $\{11.0\}/\frac{1}{3}\langle 1\bar{1}.1 \rangle$ , which contain the “basal” and “prismatic” glide plane, respectively [49]. The former allows relaxation along the direction containing the projection of the  $c$ -axis ( $x$ -axis), whereas the latter allows relaxation perpendicular to it ( $y$ -axis). For the basal system, one can determine two possible independent BURGER’s vectors  $\mathbf{b}_c$  with differing screw components but otherwise same tilt and edge components  $b_{c,\perp}$  and  $b_{c,\parallel}$ , respectively. The tilt along  $x$ -direction can then be calculated via:

$$\theta_{T,x} = \epsilon_{xx} \frac{b_{c,\perp}}{b_{c,\parallel}} = \frac{1}{\sqrt{3}} \zeta_F \epsilon_{xx}. \quad (1.16)$$

with  $\zeta_F = c_F/a_F$ . For the prismatic slip system, the possible BURGER's vectors facilitate relaxation along the  $y$ -direction via  $b_{a,\parallel}$ . But in contrast to the basal system, the tilt components  $b_{a,\perp}$  cancel out on average, thus resulting in no net tilt along the  $y$ -direction:  $\theta_{T,y} = 0$ .

**(10.0)-plane ( $m$ -orientation)** Neither basal (00.1) nor prismatic (11.0) and (10.0) slip systems can resolve strain along the  $x$ -axis: The (00.1)-plane is perpendicular to the surface and  $x$ -direction, thus the BURGER's vector can only have components in the  $y$ - $z$ -plane. But for strain release along  $x$ , the BURGER's vector should have some component in this direction, which cannot be the case. The prismatic planes, on the other hand, are perpendicular to the surface but parallel to the  $x$ -axis. This results in a dislocation line along the  $x$ -direction. To release strain, the BURGER's vector would have  $x$ -component, which does not apply for edge dislocations. So the prevailing slip system must have (01.2)-plane ( $r$ -orientation) or (11.2)-plane ( $s$ -orientation) character, which are called "pyramidal" slip systems. Three different  $r$ -planes contribute to strain release, because there is dislocation line component along the  $y$ -axis and BURGER's vector's components along the  $x$ -axis. With (1.15) and plugging in the possible BURGER's vectors one finds:

$$\theta_{T,x} = \frac{2}{3} \frac{\sqrt{3}}{\frac{20\zeta}{24+6\zeta^2} + \zeta} \left( \frac{c_S}{c_F} - 1 \right) \quad (1.17)$$

**(11.0)-plane ( $a$ -orientation)** The same argument as for the  $m$ -oriented heterostructure holds, why only pyramidal slip systems are possible. But in this case, only two  $r$ -planes contribute to strain relaxation, because the third plane is perpendicular to the surface, thus can only exhibit BURGER's vectors without in-plane components which results in no possible edge dislocations. Furthermore, in this case, the BURGER's vectors of the two remaining  $r$ -planes have opposite tilt components, i.e. they point outwards and inwards of the surface, respectively. Regarding (1.15), this will result in no net tilt of the thin film.



# Chapter 2

## Experimental Methods

### 2.1 Pulsed Laser Deposition

PLD is a Physical Vapor Deposition (PVD) technique, which essentially utilizes absorption of laser energy by a target and subsequent condensation of evaporated target material on a substrate. Like MBE or CVD, it is used for deposition of thin film materials. Although not true in general [51], a stoichiometric transfer of target composition to the substrate is attributed to PLD. In the following, the PLD setup used for this work (Fig. 2.1a) is described. Furthermore, an overview of the basic physical processes interplaying during a PLD process is given, based on Lorenz (2019) [51].

#### 2.1.1 Setup

The desired thin film material is provided by a ceramic pellet of the respective compound called “target”. It is fabricated by pressing powder with high pressure into cylindrical form, before it is sintered at high temperatures. The crystal growth takes place on a substrate, whose material is chosen to be sapphire ( $\text{Al}_2\text{O}_3$ ) of different crystal orientation, because it matches the symmetry of the here investigated sesquioxides. These quadratic slabs are 500  $\mu\text{m}$  thick with an edge length of 5 mm. In this work, oxygen is chosen as background gas to ensure fabrication of oxide thin film materials. To control the partial pressure of the background gas, the process takes place in a vacuum chamber, called PLD chamber. Inside the chamber, a target holder is placed opposite a sample holder, which both are capable of carrying up to four pellets and substrates, respectively. The latter is equipped with a resistive heater, allowing growth temperatures above 700  $^\circ\text{C}$ . To ensure homogenous ablation and deposition, both target and substrate can be rotated, whereby a frequency of 60  $\text{min}^{-1}$  is chosen in this work. Furthermore, an offset  $\varepsilon$  between the rotation centers of target and substrate is applied, i.e. the plasma plume does not hit the center of the substrate. To achieve homogeneous thickness distributions of the deposited material,  $\varepsilon = 7.5 \text{ mm}$  is chosen. Outside the PLD chamber, a KrF excimer laser produces pulsed radiation, which is redirected by a mirror and enters the chamber through a fused silica window. With a wavelength of 248 nm, a UV lens is needed to project the beam on the target surface, where the laser energy is absorbed. By repositioning the lens, the laser spot size can be controlled. The energy per pulse can be adjusted and is several hundred mJ with a duration of about 20 ns, resulting in thousands of  $\text{kW cm}^{-2}$  on the target surface [51].

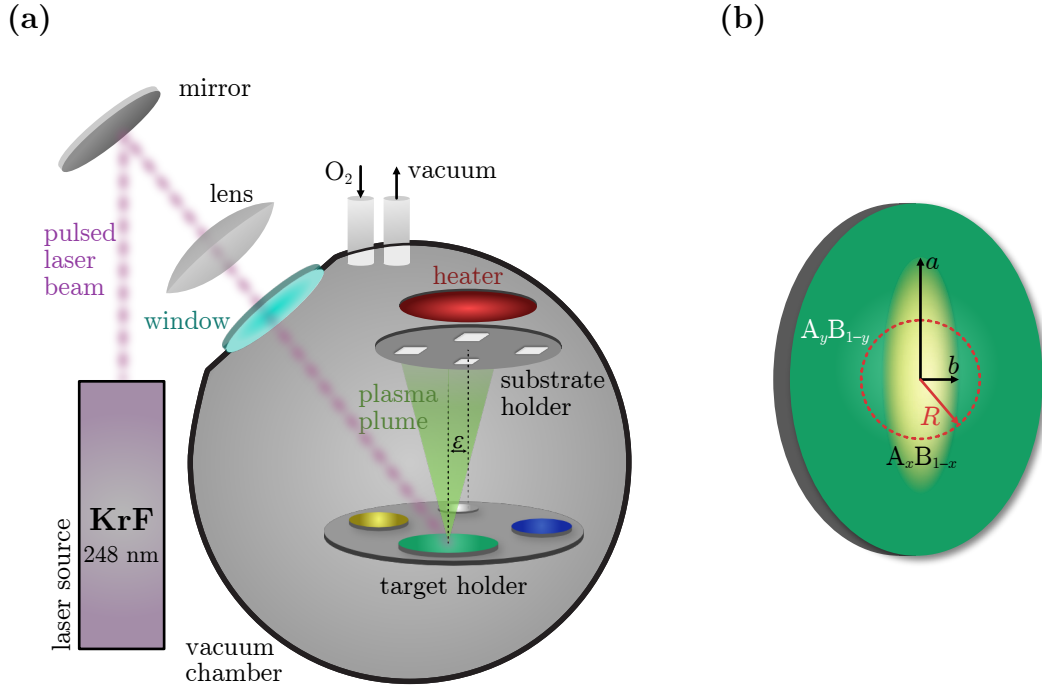


**Figure 2.1:** (a) Schematic of a PLD setup as described in 2.1.1 (b) Schematic of an elliptically segmented pellet used as target for VCCS-PLD (cf. 2.1.3).  $a$  and  $b$  are semi-major and semi-minor axis of the ellipse, respectively.  $R$  denotes the radius of the circular laser spot path on the target surface. The composition of the inner and outer segment is  $A_xB_{1-x}$  and  $A_yB_{1-y}$ , respectively.

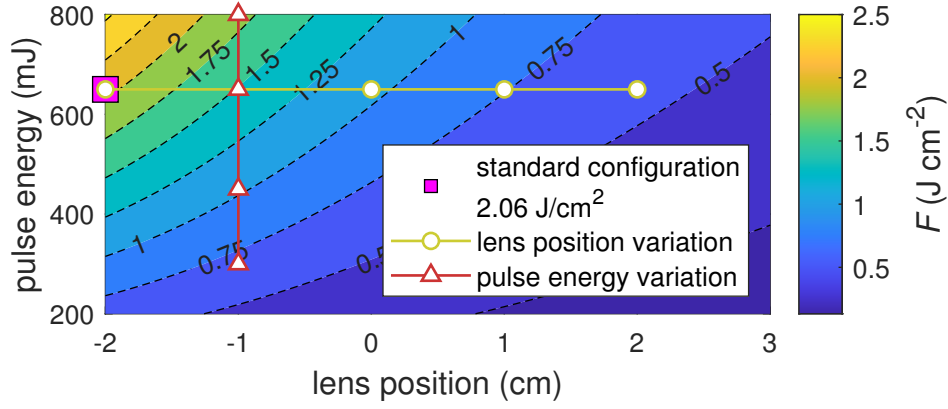


**Figure 2.2:** Laser energy density depending on the applied pulse energy and lens position. Smaller lens positions yield smaller spot sizes. A value of  $-2$  cm corresponds to the lens being as close as possible to the laser entrance window in the setup used for this work. The default configuration of  $650$  mJ and  $-2$  cm yields typical fluences of about  $2 \text{ J cm}^{-2}$ . The triangles and circles represent the variation of laser fluence in this work, achieved by varying the pulse energy and lens position, respectively.

The laser energy density, called fluence  $F$ , can be calculated by taking the energy per pulse  $E$  and the lens position  $L$  into account. For an applied  $E = 650$  mJ, 75 % of the energy are absorbed by mirror, lens and entrance window. This transmittance is assumed to be independent of  $E$ . The resulting fluence dependence  $F(E, L) = \frac{0.25E}{A(L)}$  is visualized in Fig. 2.2, whereby the laser spot size  $A$  was measured for some  $L$  and fitted by assuming parabolic behavior.

### 2.1.2 Plasma Dynamics

The PLD procedure can be broken down into three physical processes: (i) energy absorption on the target surface, (ii) formation of a plasma and (iii) condensation on the substrate:

- (i) After being projected on the surface of the pellet, the radiation penetrates the material only by a fraction of a  $\mu\text{m}$ . Electrons are excited and oscillate in the electromagnetic field of the laser pulse, which is still ongoing. Those electrons collide with bulk atoms of the surface region, which are subsequently heated up and vaporize. This process is supported by breaking of chemical bonds due to laser radiation.
- (ii) A material cloud expands perpendicular to the target surface due to Coulomb repulsion and recoil. Absorption of remaining laser radiation results in a plasma plume which is narrow for low background partial pressures below  $10^{-4}$  mbar. The target is rotated during this process to minimize the deflection of the plasma due to target degradation. The kinetic energy of the material in the plasma plume is crucial for the deposition process and can be controlled by background partial pressure and laser energy density on the target.
- (iii) The plasma plume hits the substrate which results in resputtering of already deposited material, which condensates together with the plasma, resulting in ther-



mal equilibrium and thus thin film nucleation. A large number of adatoms results in many nucleation centers which is responsible for smooth films.

It becomes clear, that PLD is a non-equilibrium process, making empirical optimization of growth parameters an essential part of thin film manufacturing [51].

### 2.1.3 Segmented Target Approach

To provide a discrete material library – a set of different samples with homogeneous composition each –, a segmented target approach as described in Wenckstern et al. (2020) [52] is applied. Specifically, the Vertical Continuous Composition Spread (VCCS) method utilizes a segmented target, i.e. a target with distinct regions of different material composition. By varying the laser spot position on the target, different plasma compositions can be achieved. Because the target is rotating during PLD, the material distribution must be in such a way that when the radial position  $R$  of the laser on the target changes, the average ablated composition  $\chi(R)$  changes. This can be realized with an elliptical segmentation, i.e. a target pellet with overall composition  $A_yB_{1-y}$ , but containing an inner ellipse with composition  $A_xB_{1-x}$  (Fig. 2.1b). By this means, any homogeneous composition  $A_\chi B_{1-\chi}$  with  $\chi$  between  $x$  and  $y$  can be realized with only one target.  $\chi$  is related to the path lengths of the moving laser spot on the inner and outer segment, respectively. The composition in the plasma can be calculated via [52]:

$$\chi(R) = y - (y - x) \frac{2}{\pi} \arccos \left[ \frac{1}{\delta} \sqrt{1 - \left( \frac{b}{R} \right)^2} \right] \quad (2.1)$$

where  $\delta$  and  $b$  are eccentricity and semi-minor axis of the ellipse, respectively<sup>1</sup>. Small and large  $R$  will result in a composition equal to the composition of the inner and outer segment, respectively. To model the process more accurately one has to take into account that the laser does not yield a point-like spot but rather an intensity distribution.

## 2.2 X-Ray Diffraction Measurement

As described in 1.1.2, constructive interference of incoming and scattered X-rays may give insight in the symmetry of exposed crystal structures. This can be utilized for thin film investigation and is called XRD. The XRD device used for this work, namely an *X'Pert Pro* (Malvern Panalytical Ltd.), as well as the applied scanning techniques will be presented in the following.

A sample with surface normal parallel to the  $z$ -axis of the laboratory system is exposed with X-rays at an angle  $\omega$  between sample surface and incident radiation. The diffracted radiation is measured at an angle  $\alpha_{\text{out}}$  between sample surface and detector.  $2\theta$  is used to describe the angle between outgoing beam and the extension of the incoming beam, which both span the scattering plane. It follows that  $2\theta = \omega + \alpha_{\text{out}}$ . Note that  $\theta$  in Equ. (1.9) is the same angle as half of  $2\theta$ . The scattering plane is depicted in Fig. 2.3a. The sample can be rotated by  $\phi$  (“azimuth”) and  $\psi$  around an axis parallel

<sup>1</sup>The eccentricity is defined as  $\delta = \sqrt{1 - b^2/a^2}$ , where  $a$  is the length of the semi-major axis.

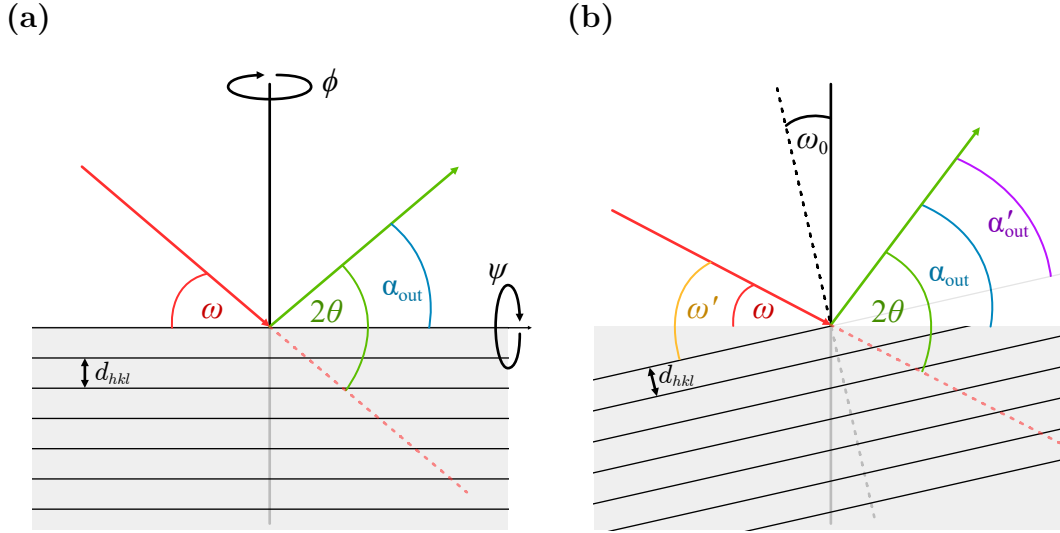


**Figure 2.3:** (a) Geometry for a  $2\vartheta$ - $\omega$ -scan without offset. (b) Scattering geometry containing an offset  $\omega_0$ . Angle of incidence and angle of diffraction decrease and increase, respectively. Note that  $2\theta$  is not affected by this offset.

to the surface normal and parallel to the intersection of sample surface and scattering plane, respectively.

### 2.2.1 $2\vartheta$ - $\omega$ -scans

When probing for lattice plane distances using the BRAGG condition in its simplest form, it is assumed that the scattering planes are parallel to the sample surface (cf. Fig. 2.3a). It is necessary that  $\omega = \alpha_{\text{out}}$  which implies  $2\theta = 2\omega$ . So the angle of incidence  $\omega$  is coupled to  $2\theta$  which represents the distance between lattice planes (cf. Equ. (1.9)). Measuring the diffracted X-ray intensity while varying  $2\theta$  and maintaining the condition  $2\theta = 2\omega$ , is called a  $2\vartheta$ - $\omega$ -scan. This results in a so-called  $2\vartheta$ - $\omega$  diffraction pattern, where peaks correspond to constructive interference and thus to certain lattice plane distances.

When analyzing  $2\vartheta$ - $\omega$  diffraction patterns, one usually compares to predicted peak positions of the expected phase of the compound which is investigated. This reference diffraction pattern stems from powder samples of the respective compound, containing all crystal orientations during one  $2\vartheta$ - $\omega$ -scan. When a peak is identified, a possible peak shift is determined and the shape of the peak is investigated. Peak shifts may be due to residual stress, substrate induced strain or compositional gradients in the thin film [2]. A minimum amount of peak broadening is always present due to convergence of the incident beam as well as convolution of  $K\alpha_1$ - and  $K\alpha_2$ -radiation (cf. 1.1.2), which is called instrumental broadening [2]. The Full Width at Half Maximum (FWHM) of the highly crystalline substrate peaks may give a reference for broadening of peaks in  $2\vartheta$ - $\omega$  diffraction data.

This method can be extended to measure lattice planes which are not parallel to the sample surface but tilted by  $\omega_0$ . This is done by rotating the reference frame of the sample in such a way that the BRAGG condition is fulfilled again. Note that  $2\theta$

does not change upon rotation, as can be seen in Fig. 2.3b. When probing for plane distances of the rotated lattice, one finds for the coupling between  $2\theta$  and  $\omega$ :

$$\begin{aligned}\omega' &= \alpha'_{\text{out}} \\ \omega + \omega_0 &= \alpha_{\text{out}} - \omega_0 \\ \omega + \omega_0 &= (2\theta - \omega) - \omega_0 \\ \Rightarrow 2\theta &= 2(\omega + \omega_0) = 2\omega' .\end{aligned}$$

This coupling is equivalent to a  $2\theta$ - $\omega$ -scan but with an offset  $\omega_0$  applied to the angle of incidence. There are several use cases for applying an offset  $\omega_0$ :

- (i) It is assumed that  $\omega$  denotes the angle between incident X-ray beam and the sample surface. But a perfect alignment between sample and sample holder is not always possible. So to correct this tilt between expected sample position and its real inclination, the offset  $\omega_0$  can be set to really probe for lattice planes parallel to the sample surface. This is done before measuring a  $2\theta$ - $\omega$ -scan to achieve preciser results.
- (ii) When probing for lattice planes which are not parallel to the sample surface (“asymmetric reflections”), one can apply the expected inclination angle as an offset  $\omega_0$ . This is the case in Fig. 2.3b.
- (iii) When  $2\theta$  is fixed, but  $\omega_0$  is varied, a so-called  $\omega$ -scan is performed, which enables quantification of mosaicity (cf. 2.2.2).

### 2.2.2 $\omega$ -scans

Thin films may exhibit a distribution of lattice plane inclination, called mosaicity. This results in an observation of diffraction peaks for several offsets  $\omega_0$ . The mosaicity can thus be quantified by fixing  $2\theta$ , representing a certain lattice plane distance, and then vary  $\omega_0$  and measure the X-ray intensity. This is called an  $\omega$ -scan, and the FWHM of the observed diffraction pattern (also called “Rocking curve”) is a measure for the mosaicity [2].  $\omega$ -scans are particularly useful when comparing a set of thin films of varying deposition parameters to optimise growth conditions. In particular, recording Rocking curves of symmetric and asymmetric lattice planes allows the calculation of dislocation densities in the thin film [53].

### 2.2.3 $\phi$ -scans

A  $2\theta$ - $\omega$ -scan is not capable of resolving in-plane rotations of crystal domains, because the distance of lattice planes parallel to the surface are not affected. Those rotational domains can be detected by probing for lattice planes which are inclined with respect to the surface, i.e. by fixing  $2\theta$  to the expected lattice plane distance and  $\omega_0$  to the inclination angle (cf. Fig. 2.3b). Depending on the symmetry of the inspected material, constructive interference should only appear for distinct values of  $\phi$ . So by rotating the sample by  $360^\circ$  and simultaneously recording the X-ray intensity, a so-called  $\phi$ -scan (also called “Azimuth-scan”) can yield information about the existence of rotational domains. If the number of observed peaks in the  $\phi$ -scan diffraction pattern exceeds the

theoretically expected number for a single crystal, rotational domains are present [2]. Furthermore, comparing the  $\varphi$ -scan diffraction data of thin film and substrate reveals whether the film has grown with an in-plane rotation with respect to the substrate. Finally, if the thin film grows in a tilted manner on the substrate, a  $\varphi$ -scan prior to an  $\omega$ -scan can ensure the correct positioning before alignment. Then, the BRAGG condition is fulfilled for performing a  $2\vartheta$ - $\omega$ -scan.

### 2.2.4 Reciprocal Space Maps

Because the BRAGG condition is equal to the description of diffraction with  $\mathbf{k}' - \mathbf{k}$  and reciprocal space vectors  $\mathbf{K}_{hkl}$  (cf. 1.1.2), both can be used depending on context. Henceforth,  $\mathbf{k}' - \mathbf{k}$  will be denoted by the “scattering vector”  $\mathbf{q}$ . Note that  $\mathbf{k}$  and  $\mathbf{k}'$  are parallel to incoming and outgoing beam, respectively. From the definition of angles, it follows that

$$\mathbf{q} = \begin{pmatrix} q_{\parallel} \\ q_{\perp} \end{pmatrix} = \mathbf{k}' - \mathbf{k} \quad (2.2)$$

$$= \frac{1}{\lambda} \begin{pmatrix} \cos \alpha_{\text{out}} \\ \sin \alpha_{\text{out}} \end{pmatrix} - \frac{1}{\lambda} \begin{pmatrix} \cos \omega \\ -\sin \omega \end{pmatrix} \quad (2.3)$$

$$= \frac{1}{\lambda} \begin{pmatrix} \cos(2\theta - \omega) - \cos(\omega) \\ \sin(2\theta - \omega) + \sin(\omega) \end{pmatrix}. \quad (2.4)$$

From Equ. (2.4), two properties follow for the scattering vector:

$$-q_{\parallel}/q_{\perp} = -\tan \left( \omega - \frac{2\theta}{2} \right) = \tan \omega_0, \quad (2.5)$$

$$|\mathbf{q}| = \sqrt{q_{\parallel}^2 + q_{\perp}^2} = \frac{1}{\lambda} 2 \sin \theta \stackrel{\text{Bragg}}{=} \frac{1}{d_{hkl}}, \quad (2.6)$$

where the last equality of Equ. (2.6) holds, if  $\mathbf{q}$  is a reciprocal lattice vector  $\mathbf{K}_{hkl}$ . The scattering vector, together with the corresponding XRD geometry is depicted in Fig. 2.4a. Because  $2\theta$  and  $\omega$  can simultaneously be represented by  $\mathbf{q}$ , it is possible to measure intensities for several  $\mathbf{q}$ , such that a part of the reciprocal space  $Q \ni \mathbf{q}$  is mapped. Consequently, this is called a Reciprocal Space Map (RSM). According to Equ. (1.8), a peak in 2D reciprocal space  $Q$  should be observed if  $\mathbf{q}$  is a reciprocal space vector. In this case,  $\mathbf{q} = \mathbf{K}_{hkl}$  is called a “reflection”. With Equ. (2.5) one can determine  $\omega_0$  – the direction of the corresponding lattice planes<sup>2</sup>, and with Equ. (2.6) the lattice plane distance  $d_{hkl}$  can be calculated.

A  $2\vartheta$ - $\omega$ -scan corresponds to a set of  $\mathbf{q}$  with fixed direction in reciprocal space, but varying length. For scanning symmetric reflections,  $\mathbf{q}$  is parallel to the surface normal (as in Fig. 2.4a). On the other hand, an  $\omega$ -scan corresponds to a set  $\mathbf{q}$  with fixed length but varying direction. The mosaicity can therefore approximately be quantified by the broadening of a reflection perpendicular to the direction of  $\mathbf{K}_{hkl}$ . Because anisotropic strain has an effect on direction and length of inclined lattice planes, asymmetric reflections, i.e.  $\omega_0 \neq 0$ , can be deconvoluted into an in-plane and out-of-plane component.

---

<sup>2</sup>Note that the “-” in  $-q_{\parallel}/q_{\perp}$  is necessary, such that this fraction is the tangens the angle between  $\mathbf{q}$  and surface normal with correct sense of rotation.

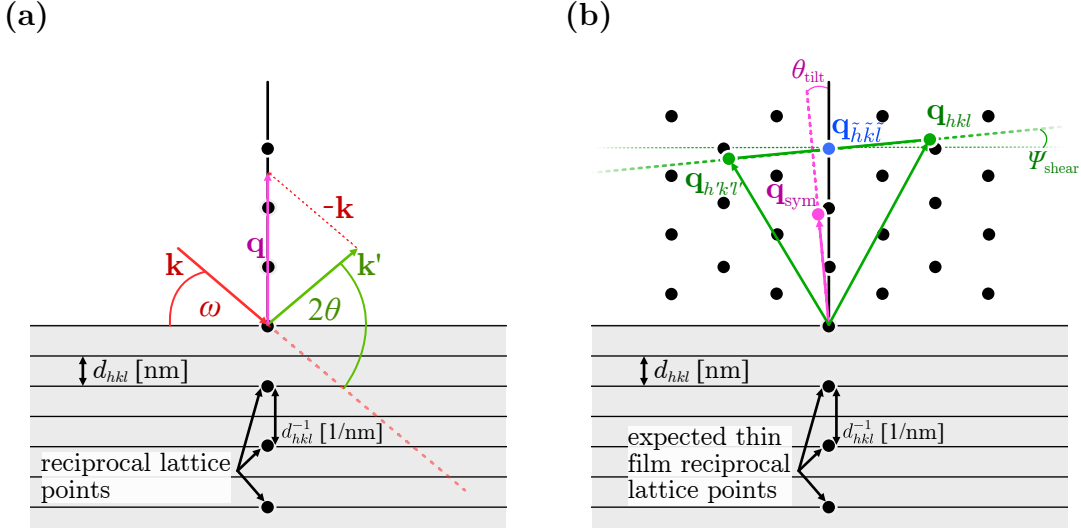


**Figure 2.4:** (a) Construction of the scattering vector (magenta) from incoming (red) and outgoing (green) beam, according to Equ. (2.4). The reciprocal lattice points are visualized together with the lattice planes. It has to be noted that the distances between lattice planes and between reciprocal lattice points have different dimensions. (b)

By this means, RSMs enable the calculation of lattice constants. To precisely calculate the latter, several corrections are applied to the recorded RSMs, as proposed in Kneiß et al. (2021) [46]:

1. High-quality sapphire substrates are used for deposition of thin films. It can be assumed that they have the expected crystal structure of bulk  $\alpha$ - $\text{Al}_2\text{O}_3$  (cf. Tab. 1.1). So any deviation of the observed reflection  $\mathbf{q}_{hkl}^{\text{Al}_2\text{O}_3, \text{obs}}$  from the expected peak position  $\mathbf{q}_{hkl}^{\text{Al}_2\text{O}_3, \text{lit}}$  is corrected by a rotation  $\mathbf{R}$  and scaling  $\rho$  of reciprocal space  $Q$ :

$$\mathbf{q}^{\text{cor}} = \rho \mathbf{R} \cdot \mathbf{q}^{\text{obs}} \quad , \quad \mathbf{q}^{\text{obs}} \in Q \quad , \quad (2.7)$$

with

$$\mathbf{R} = \begin{pmatrix} \cos \gamma & -\sin \gamma \\ \sin \gamma & \cos \gamma \end{pmatrix} \quad , \quad \gamma = \arccos \left( \frac{|\mathbf{q}_{hkl}^{\text{Al}_2\text{O}_3, \text{lit}} \cdot \mathbf{q}_{hkl}^{\text{Al}_2\text{O}_3, \text{obs}}|}{|\mathbf{q}_{hkl}^{\text{Al}_2\text{O}_3, \text{lit}}| \cdot |\mathbf{q}_{hkl}^{\text{Al}_2\text{O}_3, \text{obs}}|} \right) \quad (2.8)$$

$$\rho = \frac{|\mathbf{q}_{hkl}^{\text{Al}_2\text{O}_3, \text{lit}}|}{|\mathbf{q}_{hkl}^{\text{Al}_2\text{O}_3, \text{obs}}|} \quad . \quad (2.9)$$

2. If the thin film grows tilted (e.g. due to slip systems, cf. 1.3.2), a symmetric reflection – having scattering vector parallel to the surface normal in theory – will exhibit an in-plane component  $q_{\parallel, hkl}^{\text{film}} \neq 0$ . The tilt angle can be calculated by Equ. (2.5):

$$\theta_{\text{tilt}} = \arctan \left( -\frac{q_{\parallel, hkl}^{\text{film}}}{q_{\perp, hkl}^{\text{film}}} \right) \quad . \quad (2.10)$$

To determine the lattice constants from asymmetric peaks, the reciprocal space is again rotated as in Equ. (2.8) but with rotation angle  $-\theta_{\text{tilt}}$ . This scenario

is depicted in Fig. 2.4b, where the magenta colored reflection deviates from the expected symmetric position.

3. If the thin film is sheared, a symmetric reflection  $\mathbf{q}_{hkl}^{\text{film}}$  will be unaffected. On the contrary, an asymmetric reflection with both in- and out-of-plane component is affected. To get reliable results for the lattice constants, this shear angle  $\Psi_{\text{shear}}$  has also to be corrected, and can be calculated from two inclined lattice planes  $(hkl)$  and  $(h'k'l')$ , i.e. scattering vectors with non-zero in-plane component. Those vectors must have symmetry of a mirror plane perpendicular to the scattering plane<sup>3</sup>. The geometry is depicted in Fig. 2.4b, with the blue and green reflections representing the symmetric and asymmetric reflections, respectively. The shear angle can be calculated with

$$\Psi_{\text{shear}} = \arctan \left( \frac{q_{\perp, hkl}^{\text{film}} - q_{\perp, h'k'l'}^{\text{film}}}{q_{\parallel, hkl}^{\text{film}} - q_{\parallel, h'k'l'}^{\text{film}}} \right). \quad (2.11)$$

To correct the shear, a rotation around the corresponding symmetric reciprocal lattice point  $\mathbf{q}_{hkl}^{\text{film}}$  with the same expected out-of-plane component must be applied.

### 2.2.5 Technical Aspects

The radiation is produced by an copper anode, resulting in a wavelength of  $\lambda = 1.5406 \text{ \AA}$  for Cu-K $\alpha_1$  radiation. Note that Cu-K $\alpha_2$  and Cu-K $\beta$  radiation is not filtered out, resulting in additional low-intensity peaks in the diffractograms. Furthermore, contamination of the anode with tungsten results in an observable W-L $\alpha_1$  contribution with energy between Cu-K $\alpha$ - and Cu-K $\beta$ -radiation. During the course of the conducted experiments, the contaminated anode has been replaced, so the peaks corresponding to W-L $\alpha_1$ -radiation are not present in every diffractogram.

The diffracted radiation is detected with a *PIXcel<sup>3D</sup>* (*Malvern Panalytical Ltd.*) detector. For  $2\vartheta$ - $\omega$ -scans (cf. 2.2.1), the detector is operating in “Scanning Line” mode. For scans fixing the  $2\vartheta$  position, i.e.  $\omega$ - (cf. 2.2.2) and  $\varphi$ -scans (cf. 2.2.3), the detector is operated in “Receiving Slit” mode. RSMs are recorded with the “Frame Based” mode. The settings for the various scans are listed in Tab. 2.1. Note that it is distinguished between scans and optimizations. The latter were applied for aligning the sample correctly, depending on the measurement. For example, before a  $2\vartheta$ - $\omega$ -scan of  $m$ -plane oriented rhombohedral samples, a  $\varphi$ -scan has been applied for the inclined (30.6) reflection to find the correct azimuth of the  $c$ -axis, which is called  $\varphi$ -optimization. Afterwards, a Rocking curve has been recorded and  $\omega$  set to the maximum of the peak to compensate for the expected lattice tilt (cf. 1.3.2), called an  $\omega$ -optimization.

---

<sup>3</sup>This can be achieved by probing for a plane  $(hkl)$  and then rotate the sample around  $\phi$  by  $180^\circ$ .

**Table 2.1:** Configurations for the applied XRD scans.

scan type	detector mode	step size (°)	active channels	effective width
$2\theta$ - $\omega$ -scan	1D Scanning Line	0.005	255	$2.51^\circ$
$\omega$ -scan	0D Receiving Slit	0.005	55	3.025 mm
$\omega$ -optimization	0D Receiving Slit	0.02	37	2.035 mm
$\varphi$ -scan	0D Receiving Slit	0.05	55	3.025 mm
$\varphi$ -optimization	0D Receiving Slit	0.5	55	3.025 mm
RSMs	1D Frame Based	0.005	255	$2.51^\circ$

## 2.3 Further Methods

### 2.3.1 Thermal Evaporation

The ohmic contacts for electrical characterization of  $\text{Cr}_2\text{O}_3$  thin films were deposited by means of thermal evaporation. This method was already utilized for successfully contacting  $\alpha$ - $\text{Ga}_2\text{O}_3$  thin films [54], thus also applied for similarly structured  $\text{Cr}_2\text{O}_3$  thin films. This PVD method utilizes a “boat” made of a material with high melting temperature (tungsten W or molybdenum Mo) that is loaded with the target material in form of powder or filament. A vacuum chamber is used to achieve pressures of around  $5 \times 10^{-5}$  mbar. A high current is driven through the contacted boat, such that resistive heating ensures melting of the target material and subsequent evaporation. The evaporated material spreads out due to the pressure gradient and condensates on the sample which is mounted to a rotating holder. A metal mask ensures that only the corners of the sample are contacted.

The contacts are either a stacking of titanium, aluminum, and gold (“Ti-Al-Au”) or only titanium and gold (“Ti-Au”). The thickness of each material layer is around 30 nm, measured with a crystal oscillator during the process. The currents used for evaporating Ti, Al and Au are 60 A, 50 A and 45 A, respectively.

### 2.3.2 Resistivity Measurement

As shown by Pauw (1958) [55], it is possible to determine the specific resistivity of a flat sample by only making four small contacts at arbitrary points at its edge and measure the thickness  $t$  as well as the following resistances:

$$R_{AB,CD} = \frac{V_D - V_C}{I_{AB}} \quad , \quad R_{BC,DA} = \frac{V_A - V_D}{I_{BC}} \quad , \quad (2.12)$$

where  $V_D - V_C$  is the potential difference between points  $C$  and  $D$ , measured while applying  $I_{AB}$ , the current entering the sample at point  $A$  and leaving it at point  $B$ . The geometry<sup>4</sup> is depicted in Fig. 2.5a. The specific resistivity  $\rho$  can then be calculated

<sup>4</sup>Note that Equ. 2.13 is restricted to these conditions: “(a) The contacts are at the circumference of the sample. (b) The contacts are sufficiently small. (c) The sample is homogeneous in thickness. (d) The surface of the sample is singly connected, i.e., the sample does not have isolated holes.” (Pauw (1958) [55])



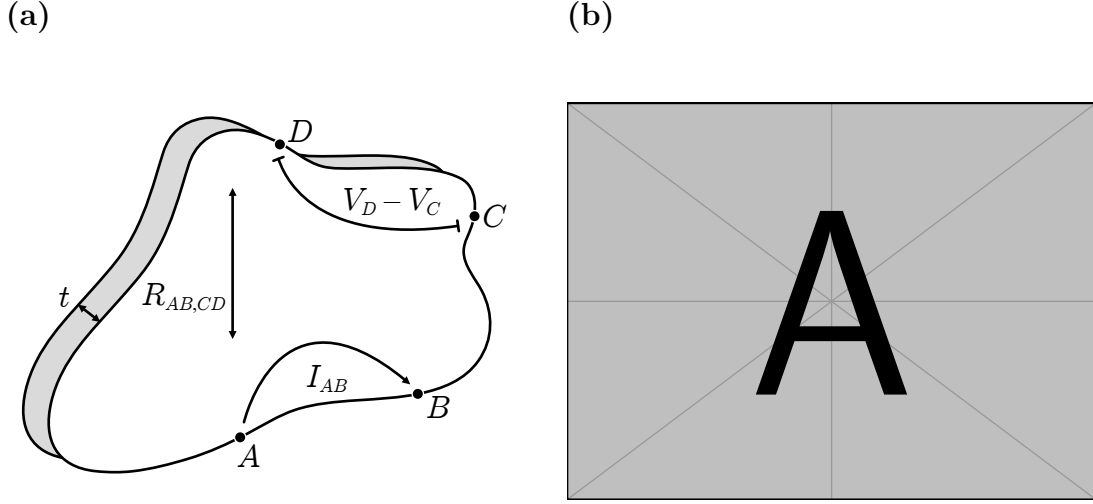


**Figure 2.5:** (a) The geometry for measuring the specific resistance as proposed by Pauw (1958) [55]. (b) Image of a 5 mm  $\times$  5 mm sample, contacted for resistivity measurements.

*tb*

via

$$\rho = \frac{\pi t}{\ln 2} \frac{R_{AB,CD} + R_{BC,DA}}{2} \cdot f \left( \frac{R_{AB,CD}}{R_{BC,DA}} \right), \quad (2.13)$$

where  $f$  is a function equal to 1, if the two measured resistances are equal;  $f$  decreases for higher ratios of the two measured resistances [55]. The geometry can further be used to determine the Hall mobility  $\mu_H$  and carrier concentration  $n$ , but due to low conductivities of the here investigated  $\text{Cr}_2\text{O}_3$  thin films, this method yields no reliable information about  $\mu_H$  and  $n$ .

Temperature-dependent resistivity measurements are conducted with a Hall probe station *CRX-VF* controlled by the measurement setup *HM-8425* (Lake Shore Cryotronics, Inc.), cooled via a *Model 336 cryogenic temperature controller* (Lake Shore). The samples are measured in a vacuum and the temperature can be controlled between 10 K and 390 K.

### 2.3.3 Thickness Determination

The optical constants and thickness  $t$  of a thin film can be measured by the change of polarization state upon light reflection. If the probing light covers several wavelengths at once, one refers to spectroscopic ellipsometry, which will be presented in the following, based on Fujiwara (2007) [56]. The incoming light can be represented by an electromagnetic wave, decomposed into two components being parallel (p) and perpendicular (s) to the scattering plane:

$$\mathcal{E} = \mathcal{E}_{\text{ip}} + \mathcal{E}_{\text{is}}. \quad (2.14)$$

In general, the amplitudes of p- and s-polarized light change in a different manner after reflection, so the overall polarization of the reflected light is changed. This change is

described by the fraction

$$\rho = \frac{r_p}{r_s} := \tan \Psi \cdot \exp(i\Delta), \quad (2.15)$$

where  $r_p$  and  $r_s$  are the amplitude reflection coefficients<sup>5</sup> for the p- and s-polarized component, respectively. For simple structures,  $\Psi$  is essentially the refractive index  $n$ , and  $\Delta$  represents the extinction coefficient  $k$ . In general, they can be calculated from the JONES-matrix – representing the reflection – and depend on the angle of incidence as well as the photon energy.

To determine the sample thickness, the spectra of  $\Psi$  and  $\Delta$  can be generated using a model for the sample structure, which is then fitted to the experimental data. In this work, this model consists of an  $\text{Al}_2\text{O}_3$  substrate without backscattering from the backside (infinite thickness); a  $\text{Cr}_2\text{O}_3$  thin film of thickness  $t$ ; and a mixed layer of air and  $\text{Cr}_2\text{O}_3$ , approximating the roughness of the sample. Because the measured spectra were confined to the visible regime of the thin film (approx.  $< 2.8 \text{ eV}$ ), one can apply the CAUCHY model [56], approximating the refractive index by

$$n(\lambda) = A + \frac{B}{\lambda^2} + \frac{C}{\lambda^4} + \mathcal{O}(\lambda^{-6}) \quad , \quad k = 0. \quad (2.16)$$

The spectroscopic ellipsometry measurements are done with an *M-2000VI* (J.A. Woolam Co., Inc.) and the data is analyzed using the software *WVASE* (J.A. Woolam). The angles of incidence are chosen to be  $50^\circ$ ,  $60^\circ$  and  $70^\circ$ , and the modelled spectral range is  $0.75 - 2.8 \text{ eV}$ . If samples of different orientation were fabricated in the same process, one can assume similar thicknesses, and a measurement with three angles was conducted only for one sample of the batch. The other samples were measured with only one angle, if the determined thickness did not differ significantly from the more accurately measured one.

Note that the investigated thin films are not isotropic in general, which is why the validity of the determined thickness is checked by profilometer measurements with a *Dektak XT Stylus Profiler* (Bruker Corporation). The edges of the quadratic substrates are masked by the sample holder during deposition, which is why they are not deposited with the target material. Consequently, measuring the height profile ranging from an edge to coated regions of the sample yields an approximation for  $t$  by the height of the observed step edge.

### 2.3.4 Spectral Transmission

---

<sup>5</sup>They are defined by the amplitude of incoming (i) and reflected (r) radiation:  $r = |\mathcal{E}_r|/|\mathcal{E}_i|$ .

# Bibliography

- [1] Neil W. Ashcroft and N. David Mermin. *Solid State Physics*. Saunders College Publishing, 1976. 826 pp.
- [2] George F. Harrington and José Santiso. “Back-to-Basics tutorial: X-ray diffraction of thin films”. In: *Journal of Electroceramics* 47.4 (2021), pp. 141–163. ISSN: 1385-3449, 1573-8663. DOI: [10.1007/s10832-021-00263-6](https://doi.org/10.1007/s10832-021-00263-6).
- [3] Lothar Spieß, ed. *Moderne Röntgenbeugung: Röntgendiffraktometrie für Materialwissenschaftler, Physiker und Chemiker*. 2., überarb. und erw. Aufl. Studium. Wiesbaden: Vieweg + Teubner, 2009. 564 pp. ISBN: 978-3-8351-0166-1.
- [4] Aoife B Kehoe et al. “Assessing the potential of Mg-doped  $\text{Cr}_2\text{O}_3$  as a novel  $p$ -type transparent conducting oxide”. In: *Journal of Physics: Condensed Matter* 28.12 (2016), p. 125501. ISSN: 0953-8984, 1361-648X. DOI: [10.1088/0953-8984/28/12/125501](https://doi.org/10.1088/0953-8984/28/12/125501).
- [5] David S. Ginley, ed. *Handbook of Transparent Conductors*. Boston, MA: Springer US, 2011. ISBN: 978-1-4419-1637-2 978-1-4419-1638-9. DOI: [10.1007/978-1-4419-1638-9](https://doi.org/10.1007/978-1-4419-1638-9).
- [6] Anna Hassa, Marius Grundmann, and Holger Von Wenckstern. “Progression of group-III sesquioxides: epitaxy, solubility and desorption”. In: *Journal of Physics D: Applied Physics* 54.22 (2021), p. 223001. ISSN: 0022-3727, 1361-6463. DOI: [10.1088/1361-6463/abd4a4](https://doi.org/10.1088/1361-6463/abd4a4).
- [7] Clemens Petersen et al. “PLD of  $\alpha\text{-Ga}_2\text{O}_3$  on  $m$ -plane  $\text{Al}_2\text{O}_3$ : Growth regime, growth process, and structural properties”. In: *APL Materials* 11.6 (2023), p. 061122. ISSN: 2166-532X. DOI: [10.1063/5.0149797](https://doi.org/10.1063/5.0149797).
- [8] S.I. Stepanov et al. “HVPE growth of corundum-structured  $\alpha\text{-Ga}_2\text{O}_3$  on sapphire substrates with  $\alpha\text{-Cr}_2\text{O}_3$  buffer layer”. In: *Materials Physics and Mechanics* 47 (2021), pp. 577–581. DOI: [10.18149/MPM.4742021\\_4](https://doi.org/10.18149/MPM.4742021_4).
- [9] N. Uekawa and K. Kaneko. “Dopant Reduction in  $p$ -Type Oxide Films upon Oxygen Absorption”. In: *The Journal of Physical Chemistry* 100.10 (1996), pp. 4193–4198. ISSN: 0022-3654, 1541-5740. DOI: [10.1021/jp952784m](https://doi.org/10.1021/jp952784m).
- [10] P. S. Robbert et al. “Novel electronic and magnetic properties of ultrathin chromium oxide films grown on  $\text{Pt}(111)$ ”. In: *Journal of Vacuum Science & Technology A: Vacuum, Surfaces, and Films* 16.3 (1998), pp. 990–995. ISSN: 0734-2101, 1520-8559. DOI: [10.1116/1.581283](https://doi.org/10.1116/1.581283).
- [11] M.F. Al-Kuhaili and S.M.A. Durrani. “Optical properties of chromium oxide thin films deposited by electron-beam evaporation”. In: *Optical Materials* 29.6 (2007), pp. 709–713. ISSN: 09253467. DOI: [10.1016/j.optmat.2005.11.020](https://doi.org/10.1016/j.optmat.2005.11.020).

- [12] François Lebreau et al. “Structural, Magnetic, Electronic, Defect, and Diffusion Properties of  $\text{Cr}_2\text{O}_3$ : A DFT+ $U$  Study”. In: *The Journal of Physical Chemistry C* 118.31 (2014), pp. 18133–18145. ISSN: 1932-7447. DOI: [10.1021/jp5039943](https://doi.org/10.1021/jp5039943).
- [13] Zhishan Mi et al. “The effects of strain and vacancy defects on the electronic structure of  $\text{Cr}_2\text{O}_3$ ”. In: *Computational Materials Science* 144 (2018), pp. 64–69. ISSN: 09270256. DOI: [10.1016/j.commatsci.2017.12.012](https://doi.org/10.1016/j.commatsci.2017.12.012).
- [14] Jarnail Singh et al. “Structural, optical and electrical characterization of epitaxial  $\text{Cr}_2\text{O}_3$  thin film deposited by PLD”. In: *Materials Research Express* 6.10 (2019), p. 106406. ISSN: 2053-1591. DOI: [10.1088/2053-1591/ab3543](https://doi.org/10.1088/2053-1591/ab3543).
- [15] Chun-Shen Cheng, H. Gomi, and H. Sakata. “Electrical and Optical Properties of  $\text{Cr}_2\text{O}_3$  Films Prepared by Chemical Vapour Deposition”. In: *Physica Status Solidi (a)* 155.2 (1996), pp. 417–425. ISSN: 00318965, 1521396X. DOI: [10.1002/pssa.2211550215](https://doi.org/10.1002/pssa.2211550215).
- [16] Cecilia Guillén and José Herrero. “Structural Changes Induced by Heating in Sputtered NiO and  $\text{Cr}_2\text{O}_3$  Thin Films as  $p$ -Type Transparent Conductive Electrodes”. In: *Electronic Materials* 2.2 (2021), pp. 49–59. ISSN: 2673-3978. DOI: [10.3390/electronicmat2020005](https://doi.org/10.3390/electronicmat2020005).
- [17] M. Catti et al. “Electronic, magnetic and crystal structure of  $\text{Cr}_2\text{O}_3$  by theoretical methods”. In: *Journal of Physics and Chemistry of Solids* 57.11 (1996), pp. 1735–1741. ISSN: 00223697. DOI: [10.1016/0022-3697\(96\)00034-0](https://doi.org/10.1016/0022-3697(96)00034-0).
- [18] Larry W. Finger and Robert M. Hazen. “Crystal structure and isothermal compression of  $\text{Fe}_2\text{O}_3$ ,  $\text{Cr}_2\text{O}_3$ , and  $\text{V}_2\text{O}_3$  to 50 kbars”. In: *Journal of Applied Physics* 51.10 (1980), pp. 5362–5367. ISSN: 0021-8979, 1089-7550. DOI: [10.1063/1.327451](https://doi.org/10.1063/1.327451).
- [19] Elisabetta Arca et al. “Effect of Chemical Precursors On the Optical and Electrical Properties of  $p$ -Type Transparent Conducting  $\text{Cr}_2\text{O}_3$ :(Mg,N)”. In: *The Journal of Physical Chemistry C* 117.42 (2013), pp. 21901–21907. ISSN: 1932-7447. DOI: [10.1021/jp404230k](https://doi.org/10.1021/jp404230k).
- [20] Valerian Pishchik, Leonid A. Lytvynov, and Elena R. Dobrovinskaya. *Sapphire: Material, Manufacturing, Applications*. Boston, MA: Springer US, 2009. ISBN: 978-0-387-85694-0 978-0-387-85695-7. DOI: [10.1007/978-0-387-85695-7](https://doi.org/10.1007/978-0-387-85695-7).
- [21] M. Marezio and J. P. Remeika. “Bond lengths in the  $\alpha$ - $\text{Ga}_2\text{O}_3$  structure and the high-pressure phase of  $\text{Ga}_{2-x}\text{Fe}_x\text{O}_3$ ”. In: *The Journal of Chemical Physics* 46.5 (1967), pp. 1862–1865. ISSN: 0021-9606, 1089-7690. DOI: [10.1063/1.1840945](https://doi.org/10.1063/1.1840945).
- [22] Ruihua Cheng, C.N. Borca, and P.A. Dowben. “Selective Area Chemical Vapor Deposition of Chromium Oxides”. In: *MRS Proceedings* 614 (2000), F10.4.1. ISSN: 0272-9172, 1946-4274. DOI: [10.1557/PROC-614-F10.4.1](https://doi.org/10.1557/PROC-614-F10.4.1).
- [23] Ruihua Cheng et al. “Characterization of the native  $\text{Cr}_2\text{O}_3$  oxide surface of  $\text{CrO}_2$ ”. In: *Applied Physics Letters* 79.19 (2001), pp. 3122–3124. ISSN: 0003-6951, 1077-3118. DOI: [10.1063/1.1416474](https://doi.org/10.1063/1.1416474).

- [24] Ruihua Cheng et al. “Potential phase control of chromium oxide thin films prepared by laser-initiated organometallic chemical vapor deposition”. In: *Applied Physics Letters* 78.4 (2001), pp. 521–523. ISSN: 0003-6951, 1077-3118. DOI: [10.1063/1.1343846](https://doi.org/10.1063/1.1343846).
- [25] L. Farrell et al. “Conducting mechanism in the epitaxial  $p$ -type transparent conducting oxide  $\text{Cr}_2\text{O}_3\text{:Mg}$ ”. In: *Physical Review B* 91.12 (2015), p. 125202. ISSN: 1098-0121, 1550-235X. DOI: [10.1103/PhysRevB.91.125202](https://doi.org/10.1103/PhysRevB.91.125202).
- [26] E. Arca, K. Fleischer, and I. V. Shvets. “Magnesium, nitrogen codoped  $\text{Cr}_2\text{O}_3$ : A  $p$ -type transparent conducting oxide”. In: *Applied Physics Letters* 99.11 (2011), p. 111910. ISSN: 0003-6951. DOI: [10.1063/1.3638461](https://doi.org/10.1063/1.3638461).
- [27] Alexander Polyakov et al. “Electrical properties of  $\alpha$ - $\text{Ga}_2\text{O}_3$  films grown by halide vapor phase epitaxy on sapphire with  $\alpha$ - $\text{Cr}_2\text{O}_3$  buffers”. In: *Journal of Applied Physics* 131.21 (2022), p. 215701. ISSN: 0021-8979, 1089-7550. DOI: [10.1063/5.0090832](https://doi.org/10.1063/5.0090832).
- [28] Alexander Polyakov et al. “Effects of sapphire substrate orientation on Sn-doped  $\alpha$ - $\text{Ga}_2\text{O}_3$  grown by halide vapor phase epitaxy using  $\alpha$ - $\text{Cr}_2\text{O}_3$  buffers”. In: *Journal of Physics D: Applied Physics* 55.49 (2022), p. 495102. ISSN: 0022-3727, 1361-6463. DOI: [10.1088/1361-6463/ac962f](https://doi.org/10.1088/1361-6463/ac962f).
- [29] Anna Caricato et al. “Deposition of chromium oxide thin films with large thermoelectromotive force coefficient by reactive pulsed laser ablation”. In: *Journal of Optoelectronics and Advanced Materials* 12 (2010), p. 427.
- [30] Sandhyarani Punugupati, Jagdish Narayan, and Frank Hunte. “Room temperature ferromagnetism in epitaxial  $\text{Cr}_2\text{O}_3$  thin films grown on r-sapphire”. In: *Journal of Applied Physics* 117.19 (2015), p. 193907. ISSN: 0021-8979, 1089-7550. DOI: [10.1063/1.4921435](https://doi.org/10.1063/1.4921435).
- [31] Elisabetta Arca et al. “Valence band modification of  $\text{Cr}_2\text{O}_3$  by Ni-doping: creating a high figure of merit  $p$ -type TCO”. In: *Journal of Materials Chemistry C* 5.47 (2017), pp. 12610–12618. ISSN: 2050-7534. DOI: [10.1039/C7TC03545D](https://doi.org/10.1039/C7TC03545D).
- [32] P. Kofstad and K. P. Lillerud. “On High Temperature Oxidation of Chromium: II. Properties of and the Oxidation Mechanism of Chromium”. In: *Journal of The Electrochemical Society* 127.11 (1980), pp. 2410–2419. ISSN: 0013-4651, 1945-7111. DOI: [10.1149/1.2129481](https://doi.org/10.1149/1.2129481).
- [33] A Holt and P Kofstad. “Electrical conductivity and defect structure of  $\text{Cr}_2\text{O}_3$ . II. Reduced temperatures ( $<\sim 1000^\circ\text{C}$ )”. In: *Solid State Ionics* 69.2 (1994), pp. 137–143. ISSN: 01672738. DOI: [10.1016/0167-2738\(94\)90402-2](https://doi.org/10.1016/0167-2738(94)90402-2).
- [34] Robert Schewski et al. “Epitaxial stabilization of pseudomorphic  $\alpha$ - $\text{Ga}_2\text{O}_3$  on sapphire (0001)”. In: *Applied Physics Express* 8.1 (2015), p. 011101. ISSN: 1882-0778, 1882-0786. DOI: [10.7567/APEX.8.011101](https://doi.org/10.7567/APEX.8.011101).
- [35] Kentaro Kaneko et al. “Progress in  $\alpha$ - $\text{Ga}_2\text{O}_3$  for practical device applications”. In: *Japanese Journal of Applied Physics* 62 (SF 2023), SF0803. ISSN: 0021-4922, 1347-4065. DOI: [10.35848/1347-4065/acd125](https://doi.org/10.35848/1347-4065/acd125).

- [36] S. J. Pearton et al. “A review of  $\text{Ga}_2\text{O}_3$  materials, processing, and devices”. In: *Applied Physics Reviews* 5.1 (2018), p. 011301. ISSN: 1931-9401. DOI: [10.1063/1.5006941](https://doi.org/10.1063/1.5006941).
- [37] Duyoung Yang et al. “Epitaxial growth of alpha gallium oxide thin films on sapphire substrates for electronic and optoelectronic devices: progress and perspective”. In: *Electronic Materials Letters* 18.2 (2022), pp. 113–128. ISSN: 1738-8090, 2093-6788. DOI: [10.1007/s13391-021-00333-5](https://doi.org/10.1007/s13391-021-00333-5).
- [38] Kentaro Kaneko et al. “Evaluation of misfit relaxation in  $\alpha\text{-Ga}_2\text{O}_3$  epitaxial growth on  $\alpha\text{-Al}_2\text{O}_3$  substrate”. In: *Japanese Journal of Applied Physics* 51 (2R 2012), p. 020201. ISSN: 0021-4922, 1347-4065. DOI: [10.1143/JJAP.51.020201](https://doi.org/10.1143/JJAP.51.020201).
- [39] Riena Jinno et al. “Reduction in edge dislocation density in corundum-structured  $\alpha\text{-Ga}_2\text{O}_3$  layers on sapphire substrates with quasi-graded  $\alpha\text{-(Al,Ga)}_2\text{O}_3$  buffer layers”. In: *Applied Physics Express* 9.7 (2016), p. 071101. ISSN: 1882-0778, 1882-0786. DOI: [10.7567/APEX.9.071101](https://doi.org/10.7567/APEX.9.071101).
- [40] Riena Jinno et al. “Crystal orientation dictated epitaxy of ultrawide-bandgap 5.4-to 8.6-eV  $\alpha\text{-(AlGa)}_2\text{O}_3$  on m-plane sapphire”. In: *Science Advances* 7.2 (2021), eabd5891. ISSN: 2375-2548. DOI: [10.1126/sciadv.abd5891](https://doi.org/10.1126/sciadv.abd5891).
- [41] Anna Hassa et al. “Control of phase formation of  $(\text{Al}_x\text{Ga}_{1-x})_2\text{O}_3$  thin films on c-plane  $\text{Al}_2\text{O}_3$ ”. In: *Journal of Physics D: Applied Physics* 53.48 (2020), p. 485105. ISSN: 0022-3727, 1361-6463. DOI: [10.1088/1361-6463/abaf7d](https://doi.org/10.1088/1361-6463/abaf7d).
- [42] L. D. Landau and E. M. Lifshitz. *Theory of Elasticity*. Course of Theoretical Physics vol. 7. Pergamon Press Ltd., 1970. 165 pp. ISBN: 978-0-08-057069-3.
- [43] Marius Grundmann. “Elastic theory of pseudomorphic monoclinic and rhombohedral heterostructures”. In: *Journal of Applied Physics* 124.18 (2018), p. 185302. ISSN: 0021-8979, 1089-7550. DOI: [10.1063/1.5045845](https://doi.org/10.1063/1.5045845).
- [44] H.L. Alberts and J.C.A. Boeyens. “The elastic constants and distance dependence of the magnetic interactions of  $\text{Cr}_2\text{O}_3$ ”. In: *Journal of Magnetism and Magnetic Materials* 2.4 (1976), pp. 327–333. ISSN: 03048853. DOI: [10.1016/0304-8853\(76\)90044-5](https://doi.org/10.1016/0304-8853(76)90044-5).
- [45] Marius Grundmann. “A most general and facile recipe for the calculation of heteroepitaxial strain”. In: *physica status solidi (b)* 257.12 (2020), p. 2000323. ISSN: 0370-1972, 1521-3951. DOI: [10.1002/pssb.202000323](https://doi.org/10.1002/pssb.202000323).
- [46] Max Kneiß et al. “Strain states and relaxation for  $\alpha\text{-(Al}_x\text{Ga}_{1-x})_2\text{O}_3$  thin films on prismatic planes of  $\alpha\text{-Al}_2\text{O}_3$  in the full composition range: Fundamental difference of a- and m-epitaxial planes in the manifestation of shear strain and lattice tilt”. In: *Journal of Materials Research* 36.23 (2021), pp. 4816–4831. ISSN: 0884-2914, 2044-5326. DOI: [10.1557/s43578-021-00375-3](https://doi.org/10.1557/s43578-021-00375-3).
- [47] Marius Grundmann. *The Physics of Semiconductors: An Introduction Including Nanophysics and Applications*. Graduate Texts in Physics. Cham: Springer International Publishing, 2016. ISBN: 978-3-319-23879-1 978-3-319-23880-7. URL: <http://link.springer.com/10.1007/978-3-319-23880-7>.
- [48] Derek Hull and D. J. Bacon. *Introduction to Dislocations*. 5th ed. Elsevier Ltd., 2011. 268 pp. ISBN: 978-0-08-096673-1.



- [49] M. Grundmann and M. Lorenz. “Anisotropic strain relaxation through prismatic and basal slip in  $\alpha$ -(Al, Ga)<sub>2</sub>O<sub>3</sub> on R-plane Al<sub>2</sub>O<sub>3</sub>”. In: *APL Materials* 8.2 (2020), p. 021108. ISSN: 2166-532X. DOI: [10.1063/1.5144744](https://doi.org/10.1063/1.5144744).
- [50] M. Grundmann, T. Stralka, and M. Lorenz. “Epitaxial growth and strain relaxation of corundum-phase (Al,Ga)<sub>2</sub>O<sub>3</sub> thin films from pulsed laser deposition at 1000 °C on r-plane Al<sub>2</sub>O<sub>3</sub>”. In: *Applied Physics Letters* 117.24 (2020), p. 242102. ISSN: 0003-6951, 1077-3118. DOI: [10.1063/5.0030675](https://doi.org/10.1063/5.0030675).
- [51] Michael Lorenz. “Pulsed laser deposition”. In: *Encyclopedia of Applied Physics*. Wiley, 2019. URL: <http://dx.doi.org/10.1002/3527600434.eap810>.
- [52] Holger von Wenckstern et al. “A review of the segmented-target approach to combinatorial material synthesis by pulsed-laser deposition”. In: *Phy. Status Solidi B* 257.7 (2020), p. 1900626. ISSN: 0370-1972, 1521-3951. DOI: [10.1002/pssb.201900626](https://doi.org/10.1002/pssb.201900626).
- [53] V. Srikant, J. S. Speck, and D. R. Clarke. “Mosaic structure in epitaxial thin films having large lattice mismatch”. In: *Journal of Applied Physics* 82.9 (1997), pp. 4286–4295. ISSN: 0021-8979, 1089-7550. DOI: [10.1063/1.366235](https://doi.org/10.1063/1.366235).
- [54] Sofie Vogt et al. “Realization of Conductive n-Type Doped  $\alpha$ -Ga<sub>2</sub>O<sub>3</sub> on *m*-Plane Sapphire Grown by a Two-Step Pulsed Laser Deposition Process”. In: *physica status solidi (a)* 220.3 (2023), p. 2200721. ISSN: 1862-6300, 1862-6319. DOI: [10.1002/pssa.202200721](https://doi.org/10.1002/pssa.202200721).
- [55] L. J. van der Pauw. “A method of measuring specific resistivity and Hall effect of discs of arbitrary shape”. In: *Philips Research Reports* 13.1 (1958), pp. 1–9.
- [56] Hiroyuki Fujiwara. *Spectroscopic Ellipsometry. Principles and Applications*. Tōkyō: John Wiley & Sons, Ltd, 2007. ISBN: 978-4-621-07253-0.